Planet. Space Sci. **42**, 905 (1994): D. Grodent, V. Dols, J. C. Gérard, *J. Geophys. Res.* **101**, 2163 (1996).
18. Intensity traces across Jupiter's polar regions in closely spaced WFPC2 and FOC images in July 1994 give three times higher sensitivity to the auroral spectrum with WFPC2. The main oval also appeared narrower in the FOC images due in part to the higher threshold of detection.
19. S. K. Atreya, Y. L. Yung, T. M. Donahue, E. S. Barker, *Astrophys. J. Lett.* **218**, L83 (1977); A revised flux calibration [E. S. Barker *et al.*, *Astrophys. J.* **242**, 383 (1980)] requires the IFT footprint emission reported by Atreya *et al.* to have been more than 1 MR (an order of magnitude brighter than observed by HST WFPC2), and the aperture locations at the three times of detection would not have included the IFT footprint from the locus of points in Fig. 2. The reported detections, if real, are likely to have been emission from the main oval, which was not considered.
20. J. E. P. Connerney *et al.*, *Science* **262**, 1035 (1993).
21. WFPC2 reference ovals were created from images showing complete ovals on 24 March 1995 (north) and 4 March 1995 (south). These are reference ovals, not statistical or maximum likelihood ovals, and were established as a basis for comparison with other images.
22. P. Drossart, R. Prangé, J.-P. Maillard, *Icarus* **97**, 10 (1992); Y. H. Kim, S. J. Kim, J. A. Stuewe, J. Caldwell, T. M. Herbst, *ibid.* **112**, 326 (1994); J. E. P. Connerney, T. Satoh, R. L. Baron, *ibid.* **122**, 24 (1996).
23. A. L. Broadfoot, *et al.*, *J. Geophys. Res.* **86**, 8259 (1981).
24. G. E. Ballester *et al.*, *Science* **274**, 409 (1996).
25. The wavelength dependent geometric distortion created a prism dispersion of the auroral spectrum, up to a few pixels over the south pole, in all WF4 images. With a partially rotated filter on WF3 (available after 29 July 1994) this dispersion is negligible.
26. The auroral color ratio of H_2 emissions (1557 to 1619 Å) to (1230 to 1300 Å) indicates the degree of CH_4 photoabsorption (strong below 1450 Å) and corresponding atmospheric column above the auroral emissions, defined by Y. L. Yung, G. R. Gladstone, K. M Chang, J. M. Ajello, and S. K. Srivastava [*Astrophys. J. Lett.* **254**, L65 (1982)].
27. J. T. Clarke, J. Caldwell, T. Skinner, R. Yelle, *NASA Spec. Pub. 494* (1989) p. 211.
28. J. E. P. Connerney, in *Planetary Radio Emission III*, H. Rucker, M. L. Kaiser, S. J. Bauer, Eds. (Austrian Academy of Science Press, Vienna, 1992), p. 13. O_6 magnetic field estimates include Jupiter's intrinsic field and a current sheet appropriate to the time of Voyager 1 encounter, derived from in situ measurements by the Pioneer and Voyager spacecraft.
29. Auroral ovals are quoted in units of R_J referring to the distance at which the field lines cross the projected equator.
30. T. A. Livengood, H. W. Moos, G. E. Ballester, R. Prangé, *Icarus* **97**, 26 (1992); R. Prangé *et al.*, *J. Geophys. Res.* **98**, 18779 (1993); J. C. Gérard *et al.*, *Science* **266**, 1675 (1994).
31. V. M. Vasyliunas, in *Physics of the Jovian Magnetosphere*, A. J. Dessler, Ed. (Cambridge Univ. Press, Cambridge, 1983), p. 395; D. D. Barbosa, *Planet. Space Sci.* **35**, 119 (1987).
32. R. Prangé and M. Elkhamsi, *J. Geophys. Res.* **96**, 21371 (1991).
33. M. H. Acuna, F. M. Neubauer, N. F. Ness, *ibid.* **86**, 8513 (1981).
34. F. M. Neubauer, *ibid.* **85**, 1171 (1980); J. W. Belcher, *Science* **238**, 170 (1987).
35. The identification of emissions with Io's magnetic footprint results from observing the emissions following Io's orbital motion, as well as their detection near the IFT footprint in ~20 separate WFPC2 images. The single detection and three non-detections by FOC from July 1994, reported by R. Prangé *et al.*, *Nature* **379**, 323 (1996), do not by themselves identify the feature with the IFT footprint, although when combined with the WFPC2 data and the lower FOC sensitivity this appears likely to have been footprint emission. The lead angles derived from H_3^+ footprint emissions (*21*) appear systematically larger than those reported here, a difference that is presently unresolved.
36. J. E. P. Connerney *et al.*, *Bull. Am. Astron. Soc.* **27**, 1147 (1995).
37. Y. Leblanc, G. A. Dulk, F. Bagenal, *Astron. Astrophys.* **290**, 660 (1994).
38. M. G. Kivelson *et al.*, *Science* **274**, 396 (1996).
39. The IFT footprint moves in both latitude and longitude over the course of each exposure, depending on the magnetic field mapping over time. The estimated smearing of the footprint from the expected locations in the O_6 model at the beginning and end of each exposure has been subtracted from the observed emission full width at half maximum to estimate the intrinsic width.
40. We acknowledge helpful conversations with J. Belcher, M. Kivelson, F. Bagenal, and F. Crary. This work is based on observations with the NASA/ESA Hubble Space Telescope, obtained at the Space Telescope Science Institute (STScI), which is operated by the AURA, Inc. for NASA under contract NAS5-26555. The research was supported by contract JPL 959122 from NASA's Jet Propulsion Laboratory and grant GO-5624.18-93A from the Space Telescope Science Institute to the University of Michigan.

3 July 1996; accepted 26 September 1996

Time-Resolved Observations of Jupiter's Far-Ultraviolet Aurora

Gilda E. Ballester,* John T. Clarke, John T. Trauger, Walter M. Harris, Karl R. Stapelfeldt, David Crisp, Robin W. Evans, Eric B. Burgh, Christopher J. Burrows, Stefano Casertano, John S. Gallagher III, Richard E. Griffiths, J. Jeff Hester, John G. Hoessel, Jon A. Holtzman, John E. Krist, Vikki Meadows, Jeremy R. Mould, Raghvendra Sahai, Paul A. Scowen, Alan M. Watson, James A. Westphal

Simultaneous imaging and spectroscopic observations of Jupiter's far-ultraviolet aurora covering half a jovian rotation were made on 31 May 1994. The Hubble Space Telescope Wide Field Planetary Camera 2 images revealed dramatic and rapidly changing auroral features, including discrete longitudinal structures along the auroral ovals, with variable contrast; a poleward offset in a north oval sector, showing equatorward motion near dusk; emissions polewards of the ovals, apparently co-rotating; and a bright event developing near the dawn limb. Viewing geometry effects explain the rotational intensity modulation observed by the International Ultraviolet Explorer, without intrinsic longitudinal asymmetries.

The first decade of studies of Jupiter's aurora in far-ultraviolet (FUV) H Lyman α (H-Lyα) and H_2 emissions by the Voyager spacecraft (*1*) and the International Ultraviolet Explorer (IUE) (*2*) emphasized the north aurora. These data were fitted by a low-latitude oval (reaching +60° latitude) mapping along the magnetic field lines out to the Io plasma torus at 6 jovian radii (R_J), and with an enhanced emission region fixed around magnetic System III longitude λ ~ 180° to 210° contributing to the observed rotational modulation. This interpretation suggested jovian auroral processes quite different than those on Earth, with longitudinal dependencies related to large asymmetries in Jupiter's co-rotating surface magnetic field, and associated with the torus and the inner magnetosphere. These magnetospheric regions are dominated by a co-rotating equatorial plasma sheet supplied by the torus and extending tens of jovian radii into the middle magnetosphere (*3*). Remote images of the FUV aurora obtained with the Faint Object Camera (FOC) (*4*) and the Wide Field Planetary Camera 2 (WFPC2) (*5*, *6*) on the Hubble Space Telescope (HST) are now revealing a different picture. They show high-latitude emissions mapping to the middle magnetosphere,

G. E. Ballester and J. T. Clarke, Space Physics Research Laboratory, University of Michigan, Ann Arbor, MI 48109, USA.
J. T. Trauger, K. R. Stapelfeldt, D. Crisp, R. W. Evans, V. Meadows, R. Sahai, Jet Propulsion Laboratory, Pasadena, CA 91109, USA.
W. M. Harris, J. S. Gallagher III, J. G. Hoessel, Department of Astronomy, University of Wisconsin, Madison, WI 53706, USA.
E. B. Burgh, C. J. Burrows, R. E. Griffiths, Department of Physics and Astronomy, Johns Hopkins University, Baltimore, MD 21218, USA.
S. Casertano and J. E. Krist, Space Telescope Science Institute, Baltimore, MD 21218, USA.
J. J. Hester and P. A. Scowen, Department of Astronomy, Arizona State University, Tempe, AZ 85287, USA.
J. A. Holtzman and A. M. Watson, Department of Astronomy, New Mexico State University, Las Cruces, NM 88003, USA.
J. R. Mould, Mount Stromlo and Siding Springs Observatories, Australian National University, Weston Creek, ACT 2611, Australia.
J. A. Westphal, Division of Geological and Planetary Sciences, California Institute of Technology, Pasadena, CA 91125, USA.

*To whom correspondence should be addressed. E-mail: gilda@umich.edu

without the expected longitudinal enhancements. This is also seen in near-infrared images of ionospheric H_3^+ auroral emissions (*7*), reflecting secondary emissions processes. A series of WFPC2 images obtained over about half a jovian rotation on 31 May 1994 with simultaneous IUE observations of the north aurora reveal the rotational modulation of the aurora in terms of the morphological, co-rotational, and local time properties, with implications for auroral processes and associated magnetospheric regions.

The WFPC2 imaging spanned five HST orbits (Table 1). Three exposures were made in each of orbits 2, 3, and 4, imaging the FUV emissions and reflected solar continuum. In orbits 1 and 5, the continuum was imaged. The images were reduced and calibrated following Clarke *et al.* (5). The persistent auroral emissions were observed (6), along with bright auroral event emissions near the dawn limb (Figs. 1 and 2) .

The main auroral ovals showed a series of discrete longitudinal structures, which acquired a high contrast in orbit 3 and faded again in orbit 4. These structures co-rotated with Jupiter to better than ~90%, as measured from early morning to mid-afternoon. Although such co-rotating regions were measured by Voyager within the dayside middle magnetosphere, the variable and predominantly lower degree of co-rotation of this region prevents any further identification (8). The true extent and brightness of the structures differs from what is observed because of 5° to 6° of rotational blurring during the exposures. Modeling of the rotational smearing indicates that the smallest structure observed on the north at $\lambda \sim 180°$ is consistent with a feature confined to ~5° in longitude or ~3300 km in length [its full width at half maximum (FWHM)]. This is similar to its apparent length in the images. In orbit 3, its modeled peak brightness (≤1230 Å) was ~400 kR (1 kilorayleigh = 10^9 photon cm^{-2} s^{-1} over 4π steradians), corresponding to at least ~600 kR of total H_2 UV emission. The other structures to the east of this feature had the same or twice the brightness and were about twice as extended along the oval. Aligned roughly with the brightest north structure at $\lambda \sim 155°$, there was an equatorward structure that became quite bright in orbit 4, and a weaker structure at even lower latitude. The structures were separated by ~15° to 40° and appeared conjugate in the north and south to within ~20° of the conjugate points calculated with the O_6 magnetic field model for an equatorial source at 30 R_J (9). Isolated longitudinal structures were observed in other WFPC2 images (6), but our observation of a series of structures along the ovals requires magnetospheric auroral processes for this date with a discrete distribution covering a large longitudinal sector of the middle magnetosphere. Existing models of the plasma transport in the jovian magnetosphere driven by the mass loading to the Io plasma torus predict the formation of discrete longitudinal density structures propagating radially outwards (*10*). In this scenario, the auroral processes would have been disturbed by the episodic propagation of such plasma structures through the relevant middle magnetospheric regions, which, for example, could have created velocity shears and driven field-aligned currents, or modified the strong pitch angle scattering into the loss cone.

The $\lambda \sim 90°$ to 150° sector of the north oval showed an unexpected and changing morphology. The south oval was too close to the limb to resolve these characteristics, if present. In orbits 2 and 3, the sector was offset polewards of the WFPC2 reference oval (6), showing a "kink" around $\lambda \sim 130°$ (Fig. 2, A and C). The same characteristics are seen in the other WFPC2 images obtained when Jupiter's central meridian longitude (CML) was ≤190° on 18 and 20 July 1994 (*11*). Another characteristic was observed in this sector in orbit 4. In the first image the sector was still offset, but in the last two images it moved equatorwards of the reference oval when close to dusk in local and magnetic local time (Fig. 2, C and

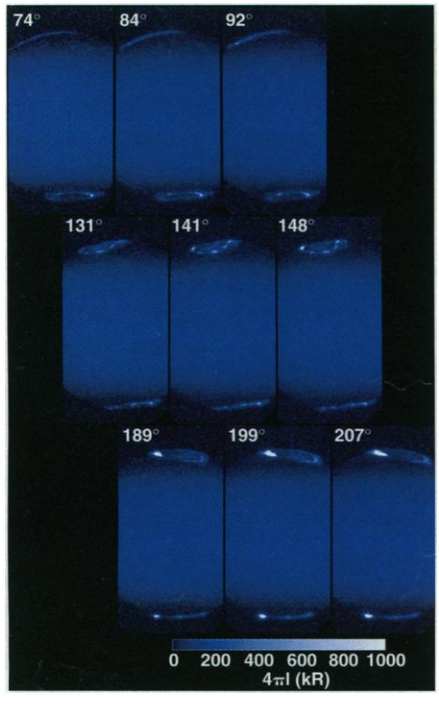

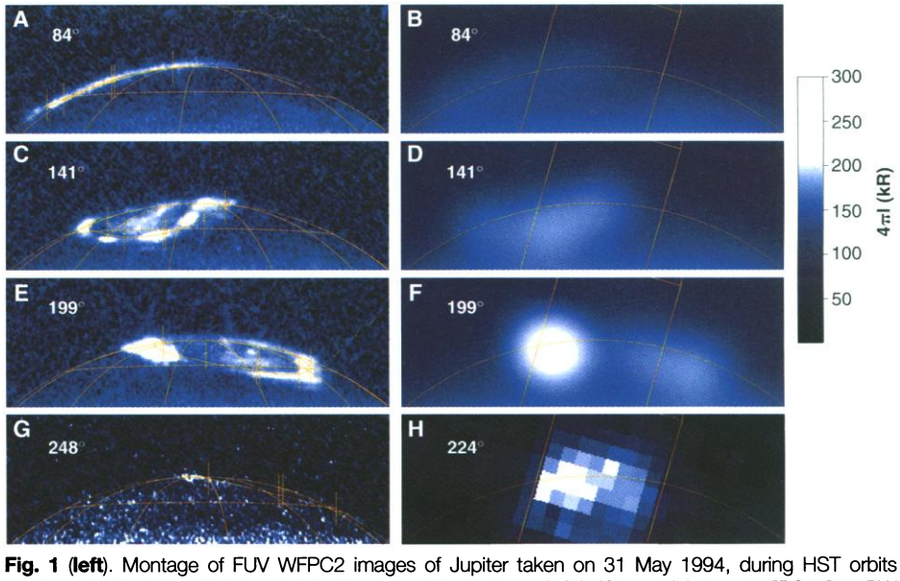

Fig. 1 (left). Montage of FUV WFPC2 images of Jupiter taken on 31 May 1994, during HST orbits numbered 2 (top), 3 (middle), and 4 (bottom). **Fig. 2 (above).** (**A**), (**C**), and (**E**) show WFPC2 F160BW images of the north aurora. (**G**) shows the F160BW + F165LP image with persistent bright event emission near dawn. Each panel has the CML indicated at the top, left, and also has overplotted: (i) Jupiter's limb and a 30° latitude/longitude grid; (ii) WFPC2 reference auroral oval at exposure midpoint; and (iii) (vertical bars) the mid-exposure location in magnetic local time of noon (2 bars), noon ± 3 hours and noon ± 6 hours (dusk, dawn), plotted if in front of the limb based on the 30 R_J O_6 auroral oval (*10*). (**B**), (**D**), and (**F**) show the WFPC2 images in the corresponding left panels after convolution with the IUE PSF, showing how the blurred emissions fall inside the approximately rectangular IUE aperture (centered at the typical +60° latitude, CML). (**H**) presents the IUE pseudo-image of H-Lyα emission at CML 224°, showing the asymmetric emission inside the IUE aperture due to the bright event emissions confined near dawn. The intensity scale (in kilorayleighs) applies to (A) through (F) and that for (G) and (H) is arbitrary.

E). A similar motion was observed in the emissions equatorwards of the sector. Although other WFPC2 images with the sector near dusk (CML ≤ 190°) show it on and off the reference oval (6), confirmation of a persistent poleward offset before the sector approaches dusk (CML ≤ 190°) should have important implications on the configuration and dynamics of Jupiter's magnetosphere resulting from the balance of the fast (10-hour) rotation and the solar wind interaction (*8, 12*).

The emissions polewards of the main north oval resembled a broad, diffuse oval. These emissions appeared to follow co-rotation with the planet within a single orbit, and the sufficiently stable morphology seen in orbits 3 and 4 allowed for confirmation, although not for measuring the departure from rigid co-rotation (Fig. 2, C and E). Co-rotation was also apparent in the 20 July 1994 WFPC2 images (*11*) and in the poleward emissions of the south aurora. In principle, the apparent co-rotation of the poleward emissions could be the result of processes associated with the co-rotating main auroral ovals. On the other hand, it could indicate association with closed magnetic field lines. In this case, the large latitudinal extent of the emissions (for example, ~15° at λ ~ 165°) maps to far regions in the dayside magnetosphere, where co-rotation should have dominated on 31 May and 20 July 1994. In Jupiter's dayside outer magnetosphere, co-rotation was measured by Voyagers 1 and 2 and Pioneer 11 when the magnetosphere was compressed, but no co-rotational flows were detected by Ulysses and Pioneer 10 when it was inflated (*8*). In addition, a small polar cap, as defined by regions poleward of the cusp mapping to open field lines swept tailward, would be implied. Although magnetic field models including only the internal and current sheet contributions yield a large polar cap within which the poleward emissions would fall (*3*), a small polar cap is predicted by models that also include the magnetopause currents (*13*).

The IUE observed the north aurora for 1.4 jovian rotations overlapping the WFPC2 imaging (Table 1). The derived IUE fluxes (*14*) showed the typical increase toward CML ~ 180° (Fig. 3), but with the peak shifted to CML ~ 248° by the dawn auroral event as previously observed for another event (*2*). To compare the IUE and WFPC2 data sets, we convolved the 0.1 arc sec resolution WFPC2 images with the IUE 3.5 arc sec point spread function (PSF) (Fig. 2) (*15*). We then spatially integrated the emissions within the IUE aperture area in the convolved WFPC2 images (*16*). These integrated emissions were found to agree within ~25% with the derived IUE fluxes (Fig. 3).

In the convolved WFPC2 images, the behavior of the normal aurora inside the IUE aperture was easily separated from that of the bright event near dawn (Fig. 2). The north oval was offset and tilted from Jupiter's rotational axis toward λ ~ 160° because of the magnetic field asymmetry. As the planet rotated, a larger portion of the aurora entered the IUE aperture. When the oval faced Earth, a bright diffuse region resulted from the blurring of the oval and poleward emissions by IUE. The best centering of this region within the IUE aperture occurred around a CML of 180°, at which point IUE normally detects peak emission. This blurred view of the high-latitude aurora explains the rotational modulation of the emission typically observed with IUE, without requiring the intrinsic longitudinal brightening around λ ~ 180° (*17*). For each IUE observing run, the exact peak CML varies because of the specific viewing geometry and auroral morphology (*6*). Similarly, the smaller rotational modulation of the south aurora usually observed with IUE (*2*) should result from the oval's smaller offset and asymmetry with respect to the rotational axis (*6*).

The 31 May 1994 WFPC2 images revealed a bright auroral event near the dawn limb that started by 13:55 UT (universal

Table 1. Exposure information for HST and IUE observations. All WFPC2 images used the sodium Woods filter F160BW, sensitive to H-Lyα and H_2 emissions (~1150 to 1680 Å) and reflected solar continuum (~1620 to 2100 Å), in the open configuration, or crossed with the afocal CaF_2 blocker F130LP to filter out emissions below ~1230 Å, or the suprasil blocker F165LP to image the continuum above ~1620 Å. Start time (Start *t*) for each WFPC2 exposure, always at 17 s past the listed minute. CML is for the midpoint of each exposure.

WFPC2 exposure	Filter	Start *t* (UT)	Exp *t* (s)	CML (deg)	IUE exposure	Start *t* (UT)	Exp *t* (s)	CML (deg)
					swp50942	07:54	900	276
					swp50943	08:36	900	302
					swp50944	09:19	900	328
					swp50945	10:02	900	354
u2eq0102	+F165LP	11:02	500	28	swp50946	10:47	900	21
u2eq0103	+F130LP	12:19	500	74	swp50947	11:36	900	50
u2eq0104	open	12:34	600	84	swp50948	12:34	900	86
u2eq0105	open	12:47	600	92				
u2eq0106	+F130LP	13:53	500	131	swp50949	13:23	900	115
u2eq0107	open	14:08	600	141	swp50950	14:10	900	144
u2eq0108	open	14:21	600	148	swp50951	14:51	900	169
u2eq0109	+F130LP	15:29	500	189				
u2eq010a	open	15:45	600	199	swp50952	15:43	900	200
u2eq010b	open	15:58	600	207	swp50953	16:24	900	224
u2eq010c	+F165LP	17:06	500	248	swp50954	17:04	900	249
					swp50955	17:45	900	274
					swp50956	18:25	900	298
					swp50957	19:04	1200	323
					swp50958	19:49	1200	350
					swp50959	20:35	1200	18
					swp50960	21:20	1200	45

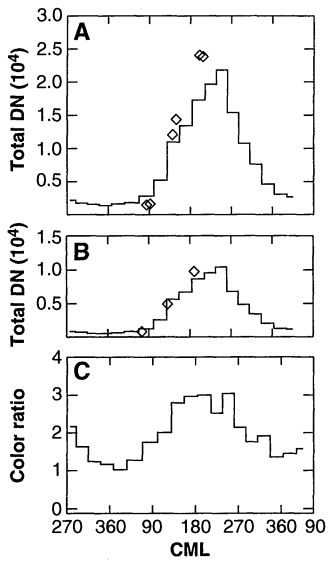

Fig. 3. (**A**) North aurora emission fluxes versus CML measured with IUE, after these were weighted by the average throughput of the HST optical telescope assembly, the WFPC2 response, and the F160BW filter transmission (solid line), plotted against the counts spatially integrated inside the IUE aperture in the WFPC2 images convolved with the IUE PSF (diamonds). The difference in the slopes of the two results is due to an underestimate of the HST + WFPC2 + F160BW response, and serves as cross-calibration. (**B**) Same as in the left panel but for the F160BW + F130LP filter combination. (**C**) H_2 color ratios versus CML derived from the IUE spectra, given by the ratio of the H_2 emission flux at 1550 to 1620 Å versus at 1230 to 1300 Å, and indicative of CH_4 absorption below 1450 Å. The usual magnitude and rotational modulation of the north aurora color ratio are observed (*2, 14*), with a maximum of ~3 around CML ~180°.

time), the beginning of orbit 3, and brightened in orbits 4 and 5. The emissions started at the latitude of the main ovals and expanded longitudinally and equatorwards, mapping out to several R_J in the middle and inner magnetosphere. The peak intensities on both poles increased by a factor of ~9 in 1.8 hours (*18*). The peak brightness detected in orbit 4 reached ~3 MR, corresponding to at least 420 erg cm^{-2} s^{-1} of local energy input at a 10% conversion efficiency (*2*). One effect of this large energy input could be to alter the CH_4 absorption ($\lesssim$1450 Å) of the H-Lyα and H_2 emissions that is normally observed in the UV auroral emissions because these are excited near the CH_4 homopause. This CH_4 absorption increased for two previous jovian auroral events observed on 21 December 1990 with IUE (*2, 19*) and on 17 July 1993 with FOC and IUE (*20, 21*), whereas we found that it remained within normal values for the May 1994 event (Fig. 3). Although a lower altitude of excitation in the two previous events, due for example to more energetic incident particles, could explain the increase of the CH_4 absorption, the situation may be more complex here, since upwelling of additional CH_4 from deeper layers may balance losses by winds and chemistry induced by the large energy input. This should depend on the altitude of excitation and the time response (*2, 14, 20, 21*).

There is evidence for a local time dependence to these events. The event peak emission on the north was separated from the limb, and moved in the sense of the planetary rotation but appeared to lag corotation by ~30% from orbit 3 to 4 (*22*). The south event emissions remained closer to the limb, as would be expected from conjugacy to the north peak longitudes (*9*). Instead of being dominated by co-rotation (*20*), the motion of the north peak emissions may have reflected its confinement to magnetic dawn, within the uncertainty in the O_6 magnetic field model (*6, 9*). Mapping the field lines at dawn from an equatorial distance of 30 R_J into the polar regions, shows that the location of the north dawn footprint was in front of the limb, near the location of the peak emission, and moving in the sense of the planetary rotation (Fig. 2, A, C, and E) (*22*). Furthermore, the continuum WFPC2 image taken in orbit 5 clearly showed extended low signal-to-noise features near dawn on both poles, presumably due to bright event H_2Lyman band and *a-b* continuum emissions longward of 1620 Å filtering through the blue tail of the F165LP blocker (Fig. 2G). At this time, the dawn footprint mapped behind the morning limb. This indicates that the brightest event emissions persisted near dawn. The IUE data support this conclusion. Auroral H-Lyα emission dominates at 1216 Å, and we have obtained nearly monochromatic H-Lyα images from the IUE data (*23*). These IUE pseudo-images show bright event emissions near dawn separated from the normal auroral emissions at CMLs of 200°, 224° (Fig. 2H), 249°, 274°, and 298°. At CML of 274°, the IUE fluxes started to decrease, but the event continued since the fluxes were all higher than in the previous rotation by a factor decreasing from 6.9 to 1.5. Modeling of the emission morphology is needed to assert if this decrease was mainly due to the event decay phase (*24*). Additional evidence is provided by the FOC images of the July 1993 event, observed at different longitudes (*20, 22*), and by the IUE pseudo-images obtained for this and the December 1990 event that also show bright emissions near dawn (*21*).

The confinement of auroral event emissions near dawn suggests the possibility of a solar wind influence on auroral events, as previously inferred from the coincidence of the December 1990 event with the expected arrival of a solar wind disturbance (*19, 20*). We find, however, no solar wind disturbance associated with the May 1994 event, based on solar wind data measured at Earth and by the Galileo Orbiter (*25*). Although a relationship between the solar wind and the December 1990 event cannot be ruled out, the average conditions found for the May 1994 event preclude a strong correlation of solar wind perturbations and auroral events. The event characteristics may be associated instead with impulsive, internally driven processes related to the configuration of the jovian magnetosphere in the dawn and predawn sector. For example, existing magnetospheric models predict reconnection in the predawn sector with sporadic merging enhancements and the accompanying injection of plasma (*12*).

REFERENCES AND NOTES

1. A. L. Broadfoot *et al.*, *Science* **204**, 979 (1979); B. R. Sandel *et al.*, *ibid.* **206**, 962 (1979); A. L. Broadfoot *et al.*, *J. Geophys. Res.* **86**, 8259 (1981); F. Herbert, B. R. Sandel, A. L. Broadfoot, *ibid.* **92**, 3141 (1987).
2. J. T. Clarke *et al.*, *Astrophys. J.* **241**, L179 (1980); T. E. Skinner, S. T. Durrance, P. D. Feldman, H. W. Moos, *ibid.* **278**, 441 (1984); G. R. Gladstone, T. E. Skinner, *NASA Spec. Pub. SP-494* (1989), pp. 221–228; T. A. Livengood, D. F. Strobel, H. W. Moos, *J. Geophys. Res.* **95**, 10375 (1990); T. A. Livengood, H. W. Moos, *Geophys. Res. Lett.* **17**, 2265 (1990); R. M. Prangé, M. Elkhamsi, *J. Geophys. Res.* **96**, 21371 (1991); T. A. Livengood, H. W. Moos, G. E. Ballester, R. M. Prangé, *Icarus* **97**, 26 (1992).
3. M. Acuña, K. W. Behanon, J. E. P. Connerney, in *Physics of the Jovian Magnetosphere*, A. J. Dessler, Ed. (Cambridge Univ. Press, New York, 1983), pp. 1–50; E. J. Smith, K.-P. Wenzel, *J. Geophys. Res.* **98**, 21111 (1993).
4. V. Dols *et al.*, *Geophys. Res. Lett.* **19**, 1803 (1992); J. A. Caldwell, B. Turgeon, X. M. Hua, *Science* **257**, 1515 (1992); J.-C. Gérard, V. Dols, R. M. Prangé, F. Paresce, *Planet. Space Sci.* **42**, 905 (1994).
5. J. T. Clarke *et al.*, *Science* **267**, 1302 (1995).
6. J. T. Clarke *et al.*, *ibid.* **274**, 404 (1996).
7. R. Baron *et al.*, *Nature*, **353**, 539 (1991); S. J. Kim *et al.*, *ibid.* p. 536; Y.-H. Kim *et al.*, *Icarus* **112**, 326 (1994).
8. J. W. Belcher, in *Physics of the Jovian Magnetosphere*, A. J. Dessler, Ed. (Cambridge Univ. Press, New York, 1983), pp. 68–102; M. Kane, B. H. Mauk, E. P. Keath, S. M. Krimigis, *J. Geophys. Res.* **100**, 19473 (1995); S. W. H. Cowley *et al.*, *ibid.* **101**, 15197 (1996).
9. J. E. P. Connerney, in *Planetary Radio Emissions III* (Austrian Academy of Sciences, Vienna, 1992) pp. 13–33.
10. Y. S. Yang, R. A. Wolf, R. W. Spiro, A. J. Dessler, *Geophys. Res. Lett.* **19**, 957 (1992).
11. The 20 July 1994 WFPC2 images spanned CMLs ~104° to 181° [Fig. 3, G and F (*6*)], and the 18 July 1994 image had a CML of 171° [Fig. 3E (*6*)]; the poleward offset should not be related to auroral events, since events did not occur during the 16 to 23 July 1994 comet Shoemaker/Levy 9 impact into Jupiter [(*6*); S. A. Budzien *et al.*, *Bull. Am. Astron. Soc.* **27**, 1149 (1995); S. Miller *et al.*, *Geophys. Res. Lett.* **22**, 1629 (1995)].
12. V. M. Vasyliunas, in *Physics of the Jovian Magnetosphere*, A. J. Dessler, Ed. (Cambridge Univ. Press, New York, 1983), pp. 395–453; T. W. Hill, A. J. Dessler, C. K. Goertz, *ibid.* pp. 353–394.
13. I. Engle, *J. Geophys. Res.* **97**, 17169 (1992), shows the north cusp boundary latitudinally displaced by ~5° from the magnetic axis for CML 202°, when the magnetic dipole axis is inclined toward Earth by 10° from the rotational axis.
14. Fluxes in the 1200 to 1230, 1230 to 1300, 1300 to 1550, and 1550 to 1620 Å intervals were derived following W. M. Harris, J. T. Clarke, M. A. McGrath, G. E. Ballester, *Icarus*, in press.
15. The IUE telescope has a nominal 3–arc sec Gaussian PSF [A. Boggess *et al.*, *Nature*, **275**, 377 (1978)]. We used a conservative 3.5 arc sec FWHM, and found similar results with 4.0 arc sec.
16. The disk-reflected sunlight was subtracted by using the fluxes integrated inside the IUE aperture in the convolved F160BW + F165LP images, scaled to the F160BW images by comparing average counts at the equator. The F160BW + F165LP images of orbits 1 and 5 differ somewhat at the poles, so a linear interpolation was made before subtraction.
17. A similar conclusion was reached by R. Prangé *et al.* (*J. Geophys. Res.*, in press) based on a set of FOC-IUE observations. In this WFPC2-IUE study, the photometry and morphology are more accurately compared because of WFPC2's higher sensitivity to low-level emissions.
18. The north/south peak emission ratio was about 3, but this includes large geometric effects.
19. R. Prangé *et al.*, *J. Geophys. Res.* **98**, 18779 (1993).
20. J. C. Gérard *et al.*, *Science* **266**, 1675 (1994).
21. W. M. Harris *et al.*, *Bull. Am. Astron. Soc.* **27**, 1149 (1995).
22. The event emission appeared to lag co-rotation since at CMLs of 141°, 149°, 190°, 200°, and 208°, the peak north emission was around $\lambda \sim 210°$, 210°, 228°, 227°, and 231°, respectively. The magnetic dawn footprint was at $\lambda \sim 190°$, 193°, 225°, 236°, and 245°, respectively. For the July 1993 event imaged by FOC (*20*), the reported quasi co-rotation included the increase of the leading emission edge and, at the imaged CMLs 108° to 172°, reflected the motion of the dawn footprint.
23. Low dispersion IUE exposures consisted of 110 spatial lines of spectra, with the aperture's long axis nearly perpendicular to dispersion. After camera noise and grating-scattered light subtraction (*14*), a 30 × 30 pseudo-image was extracted at 1216 Å. The centering of the aperture was uncertain by about one IUE pixel (~1 arc sec or ~1.2 Å), and was adjusted by tracing the aperture's edge with the extended geocoronal and Jupiter's disk-reflected H-Lyα background emissions.
24. Although the north dawn auroral sector falls inside the IUE aperture for CMLs of ~120° to 360° to 20° given the IUE pointing, after a CML of 270° the main oval starts to set behind the limb. Around a CML of 20° it rises again, but the dawn sector falls outside

the aperture, so IUE always observes maximum event emission around CMLs of ~150° to 270° (*2, 19, 21*).

25. With observations 1 month after Jupiter opposition, the solar wind conditions could be ballistically extrapolated from Earth to Jupiter (*19*) with IMP-8 and GEOTAIL satellite data. The solar wind measured at Earth on 19 and 20 May should have reached Jupiter on 31 May. Over 17 to 21 May, the velocity decreased from ~600 to ~400 km s^{-1}, the ram pressure was about average, and there were no significant magnetic field perturbations. The ballistic projection was confirmed (within ~1 day) with magnetometer data from the Galileo Orbiter. On May 1994, Galileo was ~1.7 AU from Jupiter at a ~17° Jupiter-sun-Galileo angle, and did not detect any magnetic field perturbations that could have reached Jupiter on ~28 to 31 May 1994 [K. Khurana, private communication (1996)].
26. We are grateful to A. Storrs at the Space Telescope Science Institute (STScI) for his efforts in scheduling these WFPC2 GTO observations and to B. McCollum and the IUE staff at Goddard Space Flight Center for scheduling and execution of the IUE observations on short notice. G.E.B. is also grateful to I. Engle, F. Bagenal, L. Ben Jaffel, R. Thorne, D. Rego, R. Clauer, and A. Ridley for helpful conversations; K. Khurana for providing the Galileo data; and the referees for helpful suggestions. This research was supported by the Jet Propulsion Laboratory 959122 and NASA ADP NAG5-3044 grants to the University of Michigan. This work was based on observations with the NASA–European Space Agency HST, obtained at the STScI, which is operated by the Association of Universities for Research in Astronomy for NASA under contract NAS5-26555.

12 July 1996; accepted 26 September 1996

Direct Imaging of the Atomic Configuration of Ultradispersed Catalysts

P. D. Nellist and S. J. Pennycook*

Direct imaging of individual catalyst metal atoms on the insulating surface of an industrial support is demonstrated. Individual platinum and rhodium atoms ultradispersed on γ-Al_2O_3 supports were imaged by high-resolution *Z*-contrast (atomic number *Z*) microscopy in a 300-kilovolt scanning transmission electron microscope. Within small clusters, the configuration of the metal atoms was seen to be constrained to match the surface structure of the γ-Al_2O_3, from which likely surface adsorption sites were deduced. A thin, extended raft of rhodium atoms was observed, mostly corresponding to one monolayer. Occasional two-atom features suggested partial dissolution into the top layers of the γ-Al_2O_3 support.

Direct observation of the atomic dispersion of a catalytic metal on its support material is essential for the understanding of catalytic activity and degradation mechanisms. The two systems presented here, platinum and rhodium supported on γ-Al_2O_3, have been extensively studied. Measurements of chemical activity (*1*) and x-ray absorption experiments (*2*) have demonstrated atomic dispersions approaching the limit of isolated metal atoms. However, to date no experimental investigations have provided definitive evidence of the metal atom configurations or their interactions with the support material (*3*). We used Z-contrast atomic-resolution imaging to directly observe the positions of the individual metal atoms on an industrial catalyst support material. Their configuration and orientation with respect to the support material can be determined, and information on their three-dimensional configuration can be extracted.

A Z-contrast image is formed in a scanning transmission electron microscope (STEM) by focusing an electron probe on the specimen and detecting electrons that scatter out to an annular dark-field detector. It is an incoherent mode that leads to a direct map of atomic locations with intensities that are strongly dependent on the atomic number Z of the observed atom (*4*). Thus, it is an excellent method for observing supported metal atoms; indeed, in a biological context, this was one of the earliest applications of STEM (*5*). Later work has shown how atoms of different atomic number can be distinguished (*6*) and how the number of atoms in a column can be determined from the quantization of image intensities (*7*). Although the contrast of single atoms in Z-contrast images is much stronger than that in conventional TEM images, which can only image particles smaller than about 1 nm in diameter under special conditions (*8*), these previous Z-contrast results were only possible through the use of very thin, low-Z supports such as amorphous carbon films. With industrially relevant supports such as SiO_2 or γ-Al_2O_3, single atom detection has not been possible until now because of the larger background scattering from these heavier supports. Nevertheless, the enhanced ability of Z-contrast imaging to distinguish between metal atoms and a support has made it a popular choice in the study of industrial catalysts. Hitherto, clusters as small as three atoms have been detectable (*9*), although the individual atoms could not be resolved.

The recently developed, high-resolution VG Microscopes HB603U 300-kV STEM (coefficient of spherical aberration of 1 mm) allows the formation of an electron probe only 0.126 nm in diameter. The resulting improved signal-to-background ratio from single atoms allows the resolution of individual metal atoms in tiny clusters on industrial catalyst supports. It is also possible in a STEM to form a bright-field (BF) image simultaneously with the Z-contrast image by detecting electrons collected by a small detector on the optical axis. By the principle of reciprocity (*10*), the BF image is identical to that which would be formed in a conventional TEM with the usual axial illumination. This image, being dominated by the support, is useful for determining the orientation of the support.

The ability of the microscope to resolve single atoms is illustrated in Fig. 1 for a sample of ultradispersed 3 weight % Pt on γ-Al_2O_3. The bright features (Fig. 1A) are clusters of Pt atoms. In many areas, the individual Pt atoms are resolved, showing that some clusters actually contain as few as two Pt atoms. The larger bright features are three-dimensional structures that are unresolved because they are not aligned accu-

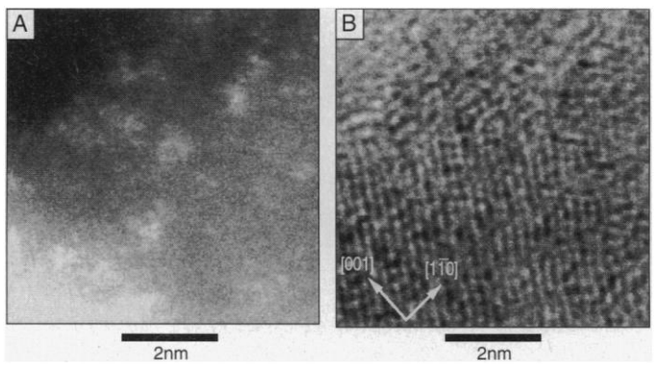

Fig. 1. Simultaneously collected (**A**) *Z*-contrast and (**B**) BF images of a sample of Pt on γ-Al_2O_3. Some of the clusters in (A) can be seen to be resolved into single atoms. In (B), strong {222} γ-Al_2O_3 fringes can be seen with a spacing of 0.23 nm.

Solid State Division, Oak Ridge National Laboratory, Oak Ridge, TN 37831–6031, USA.

*To whom correspondence should be addressed.